Characterization of a novel liquid fiducial marker for multimodal image guidance in stereotactic body radiotherapy of prostate cancer

Robin De Roover[a)]
Laboratory of Experimental Radiotherapy, Department of Oncology, KU Leuven – University of Leuven, Herestraat 49, Leuven B-3000, Belgium

Wouter Crijns and Kenneth Poels
Department of Radiation Oncology, University Hospitals Leuven, Herestraat 49, Leuven B-3000, Belgium

Ronald Peeters
Department of Radiology, University Hospitals Leuven, Herestraat 49, Leuven B-3000, Belgium

Cédric Draulans, Karin Haustermans, and Tom Depuydt[a)]
Laboratory of Experimental Radiotherapy, Department of Oncology, KU Leuven – University of Leuven, Herestraat 49, Leuven B-3000, Belgium
Department of Radiation Oncology, University Hospitals Leuven, Herestraat 49, Leuven B-3000, Belgium

(Received 6 September 2017; revised 27 February 2018; accepted for publication 27 February 2018; published 15 April 2018)

Purpose: Liquid fiducial markers have shown to be a promising alternative to solid gold markers in terms of imaging artifact reduction, patient comfort, and compatibility with different imaging modalities. This study aims to investigate the performance of the novel BioXmark® liquid marker for state-of-the-art multimodal imaging used in prostate cancer (PCa) radiotherapy, encompassing kV CT/CBCT, multiparametric MRI, and kV x-ray imaging. In addition, automatic detection of the liquid markers in x-ray imaging for prostate motion monitoring during treatment was investigated.
Methods: A total of eight BioXmark® liquid markers with varying volumes (range 5–300 μL) were casted on a square grid into a gelatin phantom insert. A cylindrical gold marker (QLRAD, length = 7 mm, Ø = 1 mm) was inserted for reference. Liquid marker visibility and streaking artifacts in CT/CBCT imaging were evaluated by placing the gelatin phantom into a CIRS anthropomorphic phantom. Relevant MRI characteristics such as the T2 and T1 relaxation times, the ADC value, and the relative proton density (ρ_H) were quantified by placing the gelatin phantom insert next to a T1MES mapping phantom and a water-filled syringe for reference. *Ex vivo* multiparametric MRI images were acquired by placing the gelatin phantom next to a resected prostate specimen. Anterior–posterior x-ray projection images were obtained by placing the gelatin phantom insert on top of an anthropomorphic pelvic phantom with internal pelvic bony structures and were acquired for five positions relative to the bony anatomy and 24 clinically relevant x-ray exposure settings. To quantify individual automatic marker detection, single markers were artificially isolated in the x-ray images using postprocessing.
Results: Markers of all sizes were clearly visible on CT and CBCT images with only the largest marker volumes (100–300 μL) displaying artifacts similar in size to the gold fiducial marker. Artifact size increased with increasing liquid marker volume. Liquid markers displayed good contrast in *ex vivo* T1-weighted and ρ_H-weighted images. The markers were not visible in the *ex vivo* T2-weighted image. The liquid markers induced a chemical shift artifact in the obtained ADC-map. Automated detection in x-ray imaging was feasible with high detection success (four of five positions) for marker volumes in the range of 25–200 μL. None of the liquid markers were detected successfully when superimposed on a bony edge, independent of their size.
Conclusions: This study is the first to show the compatibility of BioXmark® liquid markers with multimodal image-guided radiotherapy for PCa. Compared to a solid gold marker, they had favorable results in both visibility and induced imaging artifacts. Liquid marker visibility in MRI imaging of the prostate does not solely depend on the low ρ_H value (not visible on T2-weighted image) but is also influenced by its relaxation times. Automated marker detection in x-ray images was feasible but better adapted marker detection algorithms are necessary for marker localization in the presence of bony edges. Hence, the liquid marker provides a minimally invasive (fine needles) and highly applicable alternative to current solid gold markers for multimodal image-guided prostate radiotherapy treatments. [https://doi.org/10.1002/mp.12860]

Key words: liquid fiducial marker, motion monitoring, multimodal imaging, prostate radiotherapy

1. INTRODUCTION

Over the past decade, there has been growing interest in the application of stereotactic body radiotherapy (SBRT)[1,2] and focal boosting of the intraprostatic lesions[3,4] for the treatment of localized prostate cancer (PCa). Both treatments were made possible by technological advances in accurate conformal treatment delivery using image-guided intensity-modulated radiotherapy (IMRT)[5] or volumetric-modulated arc therapy (VMAT).[6] In addition, the increased usage and quality of multimodal imaging, such as computed tomography (CT), radioimmuno-guided imaging[7] and multiparametric magnetic resonance imaging (mp-MRI),[8,9] resulted in the enhanced detection and delineation of intraprostatic foci. The combination of both techniques, that is, whole-gland prostate SBRT with a simultaneous integrated boost (SIB) to the intraprostatic lesions, could improve treatment outcome while maintaining the cost-effectiveness and enhanced patient comfort offered by SBRT. However, to ensure low levels of toxicity, maintaining a high accuracy over the entire treatment delivery process is imperative.[10]

Intrafraction prostate motion is a predominant cause for treatment delivery inaccuracies as multiple studies have shown that the prostate tends to move in an unpredictable way in approximately 50% of all patients with observed motion amplitudes up to 2 cm for certain extreme cases.[11–13] The dosimetric impact of this residual intrafraction motion is non-negligible[14] and should be mitigated by accurate monitoring of the prostate position during treatment delivery.[15,16] To this end, a wide variety of motion monitoring techniques are currently utilized in clinical practice or are under development.[17–21]

Using intraprostatic fiducial markers is a widespread technique in image-guided radiotherapy (IGRT) for PCa.[22] These are mostly constructed out of materials with a high atomic number (Z), such as gold, and offer high contrast in both kV and MV x-ray imaging allowing for the (automated) detection of the prostate position. However, the necessary ultrasound-guided transrectal implantation procedure causes patient discomfort.[23,24] Moreover, gold fiducial markers cause streaking artifacts decreasing dose calculation accuracy and reduce the soft-tissue contrast on both CT and cone-beam CT (CBCT). The latter encumbers the identification of important anatomical landmarks such as the interface between rectum and prostate. The use of gold fiducial markers for image-guided proton therapy will also be hindered by the dose perturbations introduced downstream from the marker.[25,26]

Additionally, MRI imaging will be affected by the magnetic field inhomogeneity (ΔB_0) near the metallic gold markers. This inhomogeneity results in signal voids that are larger than the gold markers themselves, due to dephasing of nearby spins, and causes displacement artifacts in both the slice selection and readout directions.[27,28] Furthermore, perturbations on the apparent position in diffusion-weighted imaging (DWI) influence the accuracy of delineating the intraprostatic lesions near the implanted gold markers.[29]

The disadvantages of solid gold markers advocate the search for novel alternatives that can serve as a fiducial in multimodal image guidance, combining CT/CBCT, multiparametric MRI, and kV x-ray imaging. Such a fiducial could enhance the geometrical accuracy of the coregistration of multimodal imaging data into a single frame of reference containing all the information offered by these different imaging modalities. In this regard, liquid fiducial markers could be a promising alternative. Two liquid markers have been used for IGRT in clinical practice: Lipiodol® (Guerbet, Villepinte, France) in bladder[30,31] and prostate[32] and more recently BioXmark® (Nanovi A/S, Kongens Lyngby, Denmark) in lung.[33] The main advantages of liquid markers are a reduction in imaging artifacts[34] and a minimal perturbation of the treatment beam and dose calculation.[25] Furthermore, injection can be performed using very thin needles (typically 25G, outer diameter of 0.51 mm), potentially reducing patient discomfort. The injected volume can be varied independently from the needle size, leading to the selection of the optimal marker volume for each patient, disease site, and treatment. Both liquid markers were previously quantified in terms of their visibility in x-ray imaging and their artifact size in CT/CBCT imaging using a lung phantom showing favorable results in both aspects.[34] Additionally, Schneider et al.[35] recently demonstrated the good visibility and low level of image distortion of BioXmark® in MRI imaging using a pancreatic tissue mimicking phantom. However, all of these previous studies were focused on a single imaging modality and did not investigate the applicability of the liquid marker for a treatment that integrates multiple imaging modalities.

To this end, our study aims to investigate the performance of the novel BioXmark® liquid marker for the different imaging modalities used in state-of-the-art PCa radiotherapy. More specifically, this study examined the visibility and imaging artifacts of the liquid markers in kV CT/CBCT, mp-MRI, and kV x-ray imaging for a range of marker volumes (range 5–300 μL). Relevant MRI characteristics such as the T2 and T1 relaxation times, the apparent diffusion coefficient (ADC) and the relative proton density ρ_H were quantified. Moreover, *ex vivo* mp-MRI measurements using a prostatic specimen allowed to directly assess the visibility of the liquid markers in prostatic tissue. Finally, the applicability of the liquid marker for automated detection in kV x-ray imaging was investigated as a first step toward future use in real-time prostate motion monitoring. This study is the first to investigate the applicability of the novel liquid fiducial marker in multimodal image-guided radiotherapy for PCa.

2. MATERIALS AND METHODS

2.A. The liquid fiducial marker and gelatin phantom insert

BioXmark® (further referred to as the liquid marker) consists of a biodegradable sucrose acetate isobutyrate (SAIB), iodinated-SAIB, and ethanol solution. Mixtures of SAIB and ethanol have low viscosities allowing for injection using very thin hypodermic needles (down to 25G). Upon injection, ethanol diffusion out of the solution causes a rapid viscosity increase and formation of a highly viscous hydrophobic gel-like

marker.[36,37] To mimic the hydration reaction necessary for the formation of the gel-like markers, the BioXmark® solution was injected into water-filled glass vials. The liquid markers were subsequently casted into 10% gelatin housed in a phantom insert, the CIRS Gel Dosimetry Cassette (CIRS, Norfolk, VA, USA) [Figs. 1(a)–1(b)]. The gelatin content was chosen to be equivalent to soft tissue (ρ = 0.98 g/mL) in x-ray imaging. A total of eight different volumes (range 5–300 μL) of the liquid marker were prepared in this fashion. They were cast in the gelatin phantom insert on a square grid of 2 × 2 cm² to permit maximum distance between the different sized markers while making optimal usage of the available space (Ø: 6 cm, height: 6 cm) in the phantom [Fig. 1(c)]. A cylindrical gold fiducial marker of 7 mm length and 1 mm diameter (QLRAD, Lamaca, Cyprus) was added at the remaining ninth position in the gelatin phantom insert to act as a reference for volumetric imaging artifacts and automated detection in x-ray imaging.

2.B. CT and CBCT imaging

2.B.1. Experimental setup

KV CT and CBCT imaging were performed by placing the gelatin phantom insert into the Dynamic Pelvic Phantom (CIRS, Norfolk, VA, USA) [Fig. 1(d)]. The anthropomorphic phantom is heterogeneous, consists of tissue-equivalent material, and has a pelvic bony anatomy. One side of the phantom houses a cavity for insertion of a rotatable disk containing an off-center cubic cutout to hold dedicated inserts such as the Gel Dosimetry Cassette, which houses the gelatin phantom insert.

2.B.2. Imaging modalities and image acquisition

A planning CT scan was performed on a 40-slice Somatom Sensation Open (Siemens, Erlangen, Germany) using a high-resolution pelvis protocol. Online CBCT scans were obtained using the onboard imager (OBI) of a TrueBeam STx (Varian Medical Systems, Palo Alto, CA, USA) to inspect the impact of the liquid markers on daily volumetric IGRT. The amorphous silicon (a-Si) flat panel detector had a source to image distance (SID) of 150 cm. The scans included a pelvis CBCT and a pelvis spotlight-CBCT. Table I summarized the imaging parameters used during CT and CBCT image acquisition.

2.B.3. Data analysis

The visibility and artifact size of the liquid markers were evaluated in a qualitative manner. Artifact images ($I_{artefact}$)

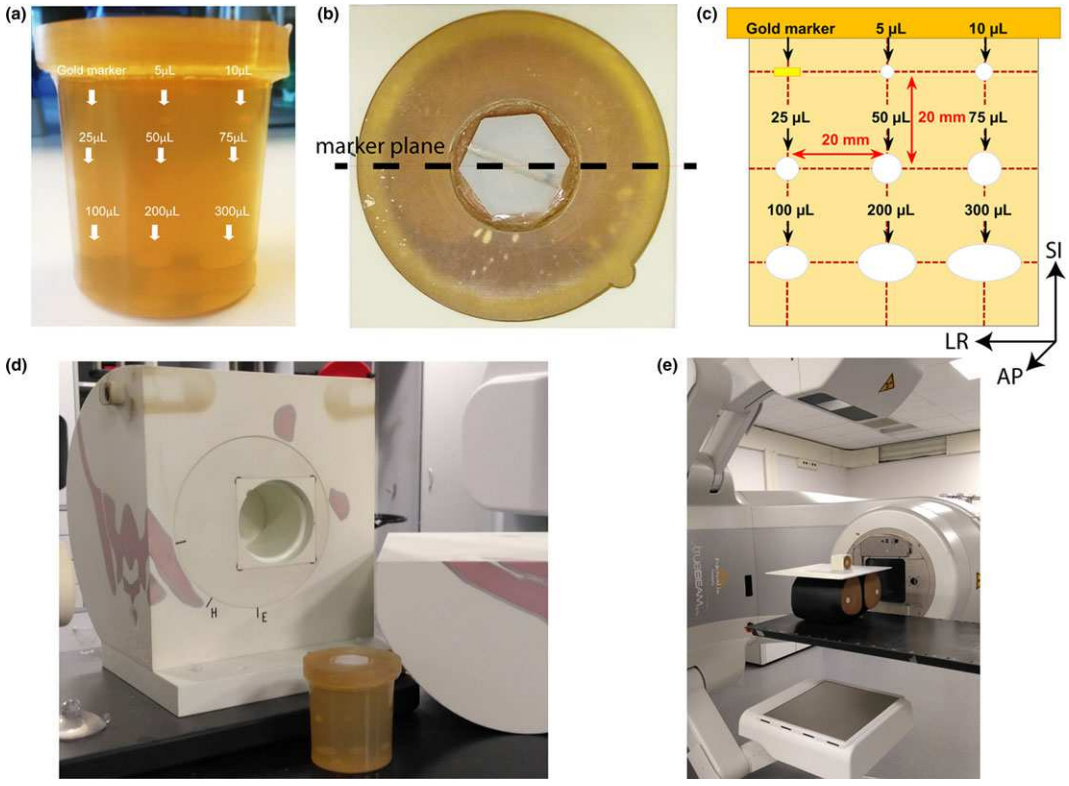

FIG. 1. (a) The gelatin phantom insert containing the liquid markers and gold fiducial marker. (b) Top view of the gelatin phantom insert denoting the plane of the 2 × 2 cm² square grid upon which the markers were casted. (c) Schematic cross section of the gelatin phantom insert showing the marker grid, the location of the eight liquid marker volumes (5–300 μL) and the gold fiducial marker. The orientation of the gelatin phantom in CT/CBCT imaging, MRI imaging, and x-ray imaging is displayed for clarity (AP direction is perpendicular to the plane). (d) Experimental setup used for CT/CBCT imaging, consisting of a CIRS anthropomorphic dynamic pelvis phantom which houses the dosimetry cassette and gelatin phantom insert. (e) Experimental setup used for anterior–posterior x-ray imaging with the kV source positioned at 0° gantry angle and the a-Si flat panel detector at 160 cm distance. The gelatin phantom insert was placed on top of a BrainLab anthropomorphic pelvic phantom and was supported by a 5 mm thick slab of water-equivalent RW3. AP x-ray images were acquired with each liquid marker positioned at the isocenter. [Color figure can be viewed at wileyonlinelibrary.com]

were constructed by subtracting the CT/CBCT slice centered at each marker plane (I_{marker}) with an adjacent slice without markers present ($I_{reference}$). Voxels that correspond to the liquid markers or the gold fiducial marker were omitted. These were determined using an HU-thresholding function on I_{marker} operating within a rectangular ROI and using a lower threshold of 500 and 3000 HU for the liquid markers and the gold marker, respectively. The contribution of image noise was removed by excluding all voxels in $I_{artefact}$ whose absolute value was below $3\sqrt{2}$ times the standard deviation of $I_{reference}$ (accounting for 99.7% of the noise in $I_{artefact}$). The respective threshold values for CT, CBCT, and spotlight-CBCT were $\Delta HU_{threshold}$ = 157/170/109 HU. This approach is similar to the one performed by Rydhög et al.[34]

The cylindrical gold marker acted as a reference for the artifacts currently observed within patients.

2.C. Magnetic resonance imaging

2.C.1. Experimental setup

All MRI measurements were performed on an Achieva 1.5 T (Philips, Amsterdam, the Netherlands) using a 16-channel SENSE XL Torso coil.

The T2 and T1 relaxation times, relative proton density (ρ_H), and ADC-map were determined by placing the gelatin phantom insert and dosimetry cassette next to a T1 mapping phantom (T1MES)[38] and a 50 mL syringe filled with water for reference.

The visibility of the liquid markers in prostatic tissue was qualitatively assessed by *ex vivo* prostate measurements. The prostate gland of a patient with histologically confirmed prostate adenocarcinoma was inserted into a prostate mold[39] after radical robotic-assisted laparoscopic prostatectomy. The prostate mold was placed inside a cylindrical housing containing formalin immediately after excision of the prostate. The cylindrical housing containing the prostate specimen was positioned next to the gelatin phantom insert and dosimetry cassette for direct comparison of the signal intensities between the prostatic tissue and the liquid markers. Multiparametric MRI images were acquired at room temperature within 24 h after excision of the prostate and consecutive formalin fixation. Written informed consent was obtained for *ex vivo* MRI measurements of the prostatectomy specimen.

2.C.2. Imaging sequences

The imaging sequences performed to generate the T2-map, T1-map, ρ_H-map, and ADC-map were:

- T2-map: a 2D multiecho spin echo (SE) sequence acquired at 32 echo times (TE) within a single repetition time (TR);
- T1-map: a 2D spin echo inversion recovery (SE-IR) sequence with 10 inversion times (TI) (TI = 30/60/100/250/400/600/900/1500/3000/5000 ms);
- ρ_H-map: a ρ_H-weighted 2D turbo spin echo (TSE) sequence with signal normalization relative to water after correcting for the T1 and T2 decay;
- ADC-map: a 2D diffusion-weighted spin echo (DWI-SE) sequence with five diffusion b-values (b-value = 0/250/500/1000/1500 s/mm²).

Ex vivo multiparametric MRI sequences included:

- T2-weighted image: a 2D TSE sequence;
- T1-weighted image: a 2D gradient echo (GRE) sequence;
- ρ_H-weighted image: a 2D TSE sequence.

No *ex vivo* DWI images were acquired as the magnetic shimming was limited to either the prostate specimen or the gelatin phantom insert.

For all sequences, frequency-encoding direction was LR, phase-encoding direction was AP, and slice selection was SI. Table II summarizes the imaging parameters used during MRI image acquisition.

2.C.3. Data analysis

The T2-map was generated by the dedicated software of the MRI scanner. Generation of the T1-map and the ADC-

TABLE I. Summary of the imaging parameters used during CT and CBCT image acquisition.

	Planning CT	Online CBCT	
Protocol	High-resolution pelvis	Pelvis	Pelvis spotlight
FOV [mm³]	362 × 362 × 228	465 × 465 × 176	262 × 262 × 186
Voxel size [mm³]	0.7 × 0.7 × 1.0	0.9 × 0.9 × 2.0	0.5 × 0.5 × 2.0
Nominal energy [kVp]	125	120	120
Tube current [mAs]	AEC	1080	750
Fan geometry	–	Half-fan	Full-fan
Rotation [°]	360	360	220
Reconstruction kernel	B30s	Ram-Lak	Ram-Lak

All volume metrics are according to LR × AP × SI.
FOV, field of view; AEC, automated exposure control.

map was performed with Matlab® R2017b (Mathworks, Natick, MA, USA) using a nonlinear least-squares fitting of Eqs. (1) and (2), respectively:

$$\text{T1-map: } S(TI_n) = |c_1|\left(1 - 2e^{-TI_n/T_1}\right), \quad (1)$$

$$\text{ADC-map: } S(b_n) = |c_2|e^{-b_n D}, \quad (2)$$

where $|c_1|, |c_2|$ are real-valued positive parameters. Polarity restoration of the signal magnitude $S(TI_n)$ was performed prior to the generation of the T1-map.[40] A quantitative ρ_H-map was determined from the ρ_H-weighted image by normalizing the signal intensity of the voxels with respect to the mean signal intensity of the water-filled syringe. The ρ_H-weighted image was corrected for the difference in T1 and T2 decay between the liquid markers and water prior to normalization. The used T1 and T2 values were obtained from their respective maps.

Voxels were determined to belong to the liquid markers if the signal intensity differed by at least 3σ (99.7% confidence) from the mean signal intensity of the gelatin phantom. This criterion was applied for the first echo of the multiecho SE sequence (TE = 12 ms), the last SE-IR sequence (TI = 5000 ms), and in the absence of diffusion gradients (b = 0 s/mm²) for the T1-map, the T2-map, and the ADC-map, respectively. The T1 and T2 relaxation time, the ADC value, and the relative ρ_H were quantified as the average value over the 25% most centrally located voxels of the largest liquid marker (300 μL) to minimize the influence of the gelatin background signal on the obtained parameter values.

Signal intensity histograms were obtained for the prostate specimen and the liquid markers to get a qualitative assessment of the visibility of the liquid markers within prostatic tissue. Voxel selection of the liquid markers used the thresholding method described above and was restricted to the 25% most centrally located voxels of the largest liquid marker. The *ex vivo* prostate was contoured manually on all slices.

2.D. X-ray imaging

2.D.1. Experimental setup

Anterior–posterior kV x-ray images were obtained by positioning the gelatin phantom insert on top of an anthropomorphic pelvic phantom (Brainlab, Munich, Germany) supported by a 5 mm thick slab of water-equivalent RW3 (PTW, Freiburg, Germany) [Fig. 1(e)]. The anthropomorphic pelvic phantom consists of water-equivalent plastic and has a pelvic bony anatomy upon which the liquid markers were superimposed in the x-ray images. The x-ray direction was perpendicular to the marker plane denoted in Fig. 1(c). Each liquid marker was positioned at the isocenter by varying the position of the gelatin phantom insert on the RW3 slab while the anthropomorphic phantom remained stationary after initial positioning. In this way, each liquid marker was superimposed on the same pelvic bony structures in the acquired x-ray images.

2.D.2. X-ray image acquisition and marker isolation

X-ray images were acquired using the OBI of a TrueBeam STx with the kV-source positioned at 0° gantry angle, a source–axis–distance (SAD) of 100 cm and a SID of 160 cm [Fig. 1(e)]. X-ray images of each liquid marker were obtained for five different positions relative to the bony structures and 24 clinically relevant exposure settings (nominal energy = 60/85/110 kVp and tube current = 0.5/1/2/5/7.5/10/15/20 mAs). The a-Si flat panel detector had a field of view (FOV) of 400 × 300 mm² with a 0.388 × 0.388 mm² in-plane pixel size. No collimation was used.

TABLE II. Summary of the imaging sequences and parameters used during MRI acquisition.

Protocol	T2-map	T1-map	ADC-map	T2-weighted	T1-weighted	ρ_H-weighted
Sequence	Multiecho SE	SE-IR	DWI-SE	TSE	GRE	TSE
Acquisition type	2D	2D	2D	2D	2D	2D
FOV [mm³]	230 × 230 × 56	180 × 180 × 56	180 × 180 × 56	230 × 230 × 53	200 × 200 × 54	230 × 230 × 53
Voxel size [mm³]	0.9 × 0.9 × 4.0	0.75 × 0.75 × 4.0	1.25 × 1.25 × 4.0	0.41 × 0.41 × 4.0	0.69 × 0.69 × 3.0	0.41 × 0.41 × 4.0
TR [ms]	5000	6000	4000	4000	200	4000
TE [ms]	12	4	88	120	5	5.7
BW/voxel [Hz]	234	361	20.6	112	220	361
Flip angle [°]	90	90	90	90	80	90
EPI factor	1	1	53	1	1	1
SENSE factor	1	1	1.5	1	1	1
Signal averages	1	1	32	2	6	1
Scan options	CLEAR	CLEAR	SPIR	–	CLEAR	–
Scan duration [s]	610	1260	1668	164	262	280

All volume metrics are according to LR × AP × SI.
FOV, field of view; BW, bandwidth; EPI, echo planar imaging; SENSE, sensitivity encoding; CLEAR, constant level appearance (homogeneity correction); SPIR, spectral presaturation with inversion recovery (fat suppression).

Artificial x-ray images containing a single marker were generated using Matlab® by removing all other markers from the image and correcting for the attenuation caused by the gelatin phantom insert at the location of the removed markers. No other postprocessing or image filters were applied.

2.E. Automated detection in x-ray images

2.E.1. Marker template generation

Marker templates were generated for each individual marker and imaging angle θ based on the planning CT image of the gelatin phantom insert using Matlab®. Voxels that correspond to the liquid markers were selected using an HU-thresholding function operating within a rectangular ROI and using a lower threshold of 500 HU for the liquid markers and 3000 HU for the gold fiducial marker. Templates were generated by a parallel projection at angle θ of the selected voxels while correcting for the attenuation of the liquid marker voxels along the projection by using its HU values obtained from the CT image. Only $\theta = 0°$ was considered for this study as the dataset only contained anterior–posterior x-ray images. The marker templates were resampled to the pixel size of the OBI (0.388×0.388 mm²).

2.E.2. Automated detection

Automated marker detection was performed offline using the normalized cross-correlation (NCC)-based template matching algorithm as implemented in Matlab® between the artificial x-ray image and the specific marker template. No ROI to limit the template matching was used.

2.E.3. Data analysis

Reference marker positions were determined by a manual delineation of each liquid marker on the x-ray image with highest liquid marker visibility (nominal energy = 110 kVp, tube current = 20 mAs). The delineation was performed three times by the same observer. The reference marker position was defined as the average centroid position of the three segmentations.

A detection was considered successful if the automatically detected position was within a 3 pixel, or 1 mm, radius with respect to the reference marker position.

3. RESULTS

3.A. CT and CBCT imaging

As shown in Fig. 2, markers of all sizes were clearly visible on the CT, pelvis-CBCT, and spotlight-CBCT images as high-intensity regions.

Liquid markers showed artifacts that were both smaller in size and less intense, that is, lower $|\Delta HU|$ values (Fig. 2), compared to the artifact created by the gold fiducial marker in the CT and CBCT images. An increase in artifact size was observed in the artifact images for larger volumes of the liquid markers. Only the largest sized markers (100–300 μL) displayed artifacts that were comparable in size to the gold fiducial marker. Liquid marker-induced imaging artifacts were most pronounced in the spotlight-CBCT.

3.B. Magnetic resonance imaging

The T2-map, T1-map, ρ_H-map, and ADC-map are visualized in Fig. 3. The mean T2 relaxation time was 521 ± 44 ms, the mean T1 relaxation time was 1390 ± 39 ms, the mean ADC value was $(1.6 \pm 0.1) \times 10^{-3}$ mm²/s, and the mean ρ_H was 37 ± 3% relative to water.

A chemical shift artifact was noticeable on the ADC-map in the phase-encoding direction [up–down in Fig. 3(d)] with an anteriorly located signal overlap and a posteriorly located signal void. The ADC-map also displayed a geometric susceptibility artifact at the air–phantom interface due to poor magnetic shimming around the gelatin phantom insert.

The *ex vivo* prostate measurements and signal intensity histograms of the prostatic tissue and the liquid markers are displayed in Fig. 4. The voxels selected to determine the histograms are segmented in Fig. 4. Based on the histograms, good contrast between prostatic tissue and the liquid markers was obtained for the T1-weighted image and the ρ_H-weighted image. The liquid markers displayed a hypointense signal in both images whose signal intensity can be clearly distinguished from the prostatic tissue. However, the T2-weighted image lacked contrast between the prostatic tissue and the liquid markers as their signal intensity histograms coincided.

3.C. Automated detection in x-ray images

An indication of the liquid marker visibility in x-ray imaging is given in Fig. 5(a). The smallest liquid markers (5–10 μL) were almost not visible whereas larger sized markers (>25 μL) were visible in the x-ray image (nominal energy = 110 kVp, tube current = 15 mAs). The signal intensity of the liquid markers was smaller compared to the signal intensity of the gold fiducial marker.

None of the liquid markers were detected successfully for all five positions as they all failed to correctly detect the marker at position 4 [Fig. 5(b)]. The latter is caused by the coincidence of the liquid marker with a bony structure edge which resulted in a decrease in the normalized cross-correlation value and a failed detection. Neglecting this position, liquid markers with a volume ranging from 25 to 200 μL had successful automated detection (four of five positions) for most exposure settings. The 5–10 μL markers lacked contrast to be detected reliably. The 300 μL marker, although clearly visible in all images, was detected less accurately by the NCC algorithm due to its large size and elongated shape, with most of its detected positions lying between a 1 mm and 3 mm radius from the reference marker position.

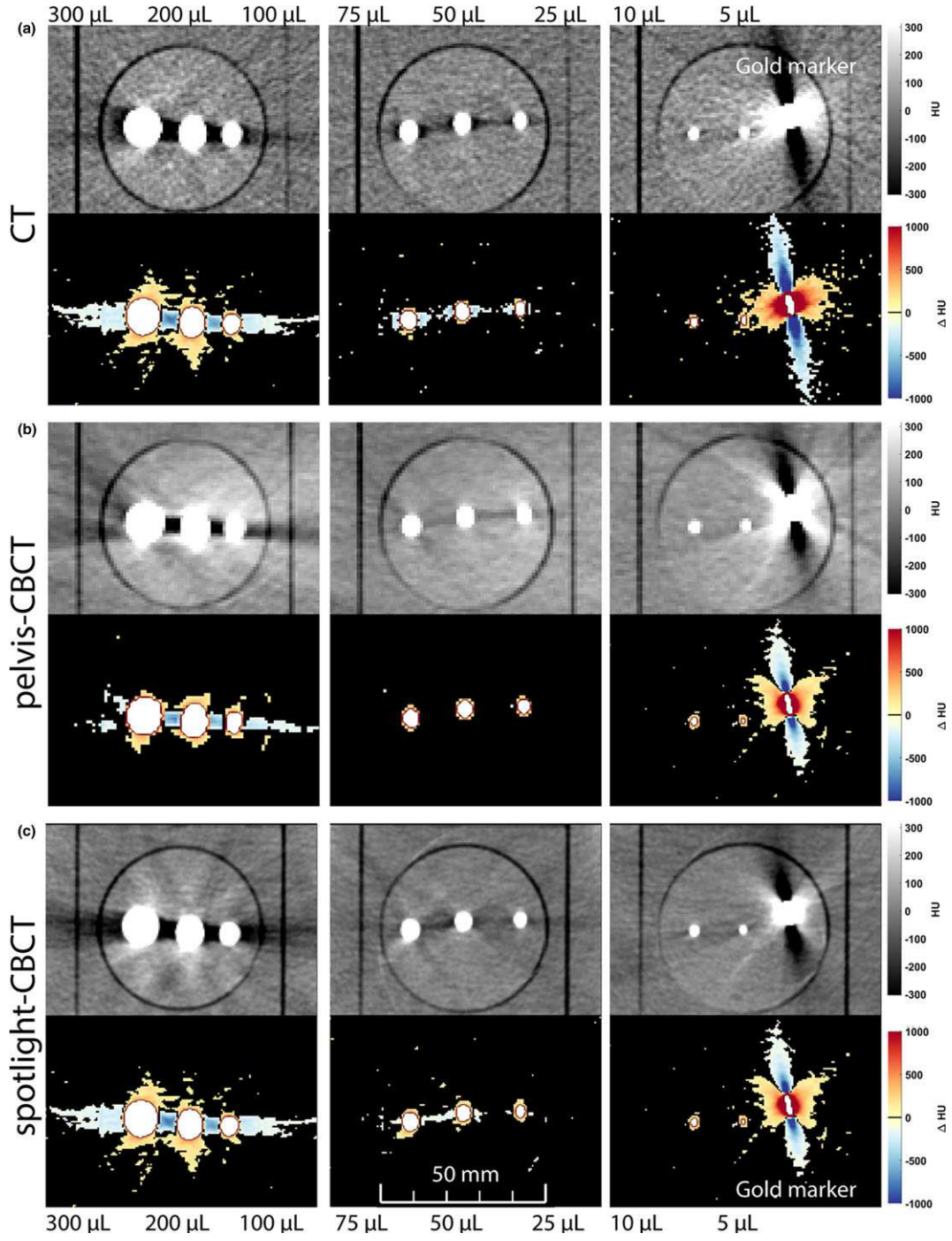

FIG. 2. Displays relevant transversal slices of the marker image I_{marker} and the artifact image $I_{artefact} = I_{marker} - I_{reference}$, for (a) the high-resolution pelvis CT (voxel size = 0.65 × 0.65 × 1 mm³), (b) the pelvis-CBCT (voxel size = 0.91 × 0.91 × 2 mm³), and (c) the pelvis spotlight-CBCT (voxel size = 0.51 × 0.51 × 2 mm³). All marker images used pelvis HU window settings (−304 to 314 HU). Voxels in $I_{artefact}$ for which $|\Delta HU|$ was below the threshold of $3\sqrt{2}$ times the standard deviation of $I_{reference}$ were removed from $I_{artefact}$ (99.7% of imaging noise). Liquid markers showed smaller artifacts compared to the gold fiducial marker both in terms of artifact size and intensity ($|\Delta HU|$). Only the largest sized markers (100–300 µL) induced artifacts that were similar in size to the gold fiducial marker. [Color figure can be viewed at wileyonlinelibrary.com]

For reference, the gold fiducial marker was detected successfully for all five positions. Failed detection of the gold fiducial marker only occurred for the lowest exposure settings (nominal energy = 60 kVp and tube current = 0.5/1/2 mAs) for which none of the positions were detected successfully.

Of the 472 failed detections, 384 were caused by a mismatch with a bony structure resembling the liquid marker in the x-ray image, which resulted in the marker being detected at a distance of more than 3 mm from the actual reference marker position. The 300 µL marker was only mismatched with a bony structure in 36 of 109 failed detections as most of

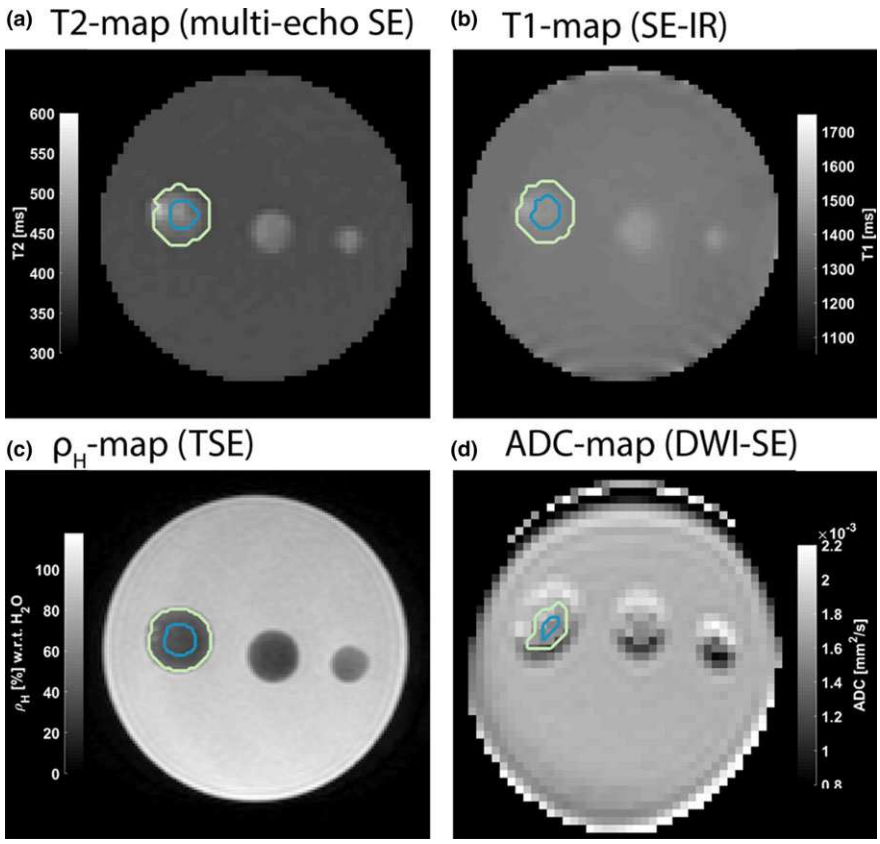

FIG. 3. (a) T2-map (voxel size = 0.9 × 0.9 × 4.0 mm³). (b) T1-map (voxel size = 0.75 × 0.75 × 4.0 mm³). (c) ρ_H-map (voxel size = 0.41 × 0.41 × 4.0 mm³). (d) ADC-map (voxel size = 1.25 × 1.25 × 4.0 mm³). The outer contours denote the voxels that belong to the largest liquid marker (300 μL) after applying the thresholding method described in Section 2.C.3. The inner contours denote the 25% most centrally located voxels of the largest marker and were used to determine the mean value of the respective MRI parameters. The ADC-map contains a chemical shift artifact in the phase encoding direction (up-down) and displays geometric distortions near the air-phantom interface. [Color figure can be viewed at wileyonlinelibrary.com]

its failed detections were caused by an inaccurate detection of the centroid position of the marker (and were in the range of 2–3 mm).

4. DISCUSSION

This study examined the applicability of a novel liquid fiducial marker for state-of-the-art PCa radiotherapy in which the use of multimodal imaging and automated motion monitoring is of increasing importance. To this end, we evaluated the visibility and imaging artifacts of eight BioXmark® liquid markers with varying volume (range 5–300 μL) in kV CT/CBCT, multiparametric MRI, and kV x-ray imaging. In addition, relevant MRI parameters such as the T2 and T1 relaxation time, the ADC value, and the relative proton density ρ_H were characterized. Individual automated marker detection in x-ray imaging was quantified to explore the feasibility of using the novel liquid marker as a fiducial for automated motion monitoring.

The artifact size on CT and CBCT imaging was previously quantified by Rydhög et al.[34] for various concentrations of the radio-opaque component of a 250 μL liquid marker. Our results confirm that the liquid marker compares favorably with solid gold markers in terms of artifact size. Moreover, the artifact intensity (measured by $|\Delta HU|$ in Fig. 2) was much smaller for the liquid markers compared to the gold marker.

Additionally, we showed that the imaging artifacts became more noticeable for increasing marker size, supporting the postulation by Rydhög et al.[34] that liquid marker artifacts are induced by their larger physical size. Only the largest markers (100–300 μL) showed imaging artifacts comparable in size to the gold fiducial marker (Fig. 2). However, the artifact size of the largest markers could be enhanced by their proximity with respect to each other (they were inserted on a 2 × 2 cm² grid displayed in Fig. 1). Interference between nearby markers potentially results in a larger artifact size when compared to the artifact induced by an isolated marker. This interference makes a quantitative comparison in terms of artifact size difficult. However, it should be noted that the spacing between intraprostatic markers can be comparable to the spacing between the liquid markers in the gelatin phantom insert. Hence, similar interference between the liquid markers and corresponding artifacts can be expected when the largest sized markers are injected into the prostate, depending on the geometry of the intraprostatic markers.

Most importantly, the reduced size and intensity of liquid marker-induced artifacts compared to solid gold markers will be beneficial for identifying relevant anatomical landmarks, such as the interface between the prostate and the rectum, in

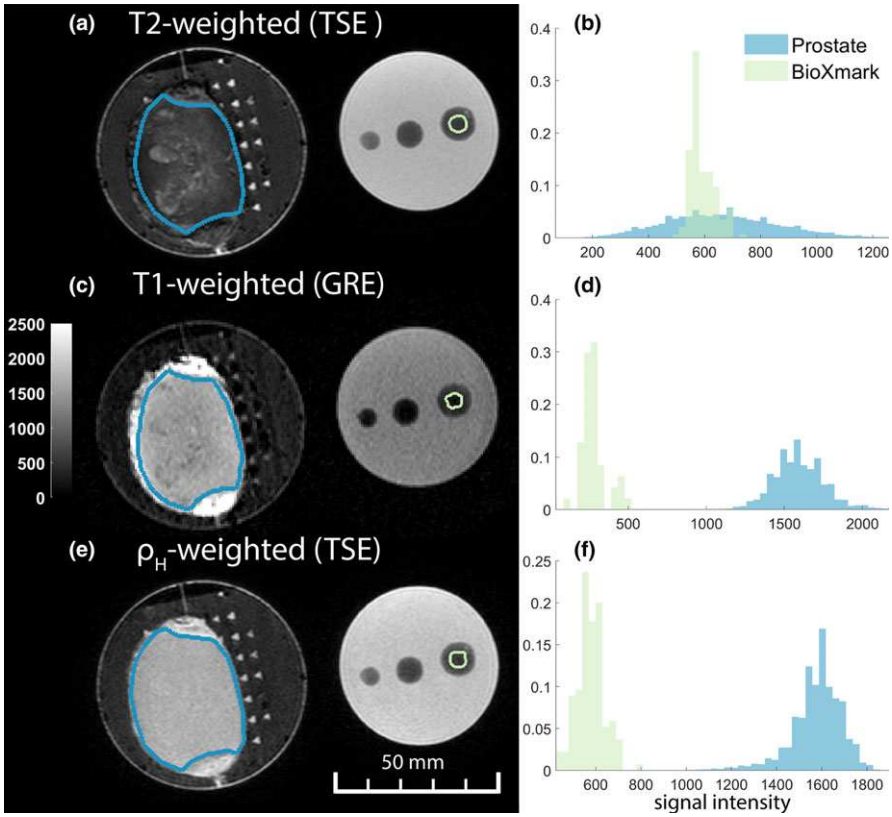

FIG. 4. Visualizes the ex-vivo prostate measurements and the corresponding signal intensity histograms for: (a)–(b) T2-weighted image (voxel size = 0.41 × 0.41 × 4.0 mm³); (c)–(d) T1-weighted image (voxel size = 0.69 × 0.69 × 3.0 mm³); (e)–(f) ρ_H-weighted image (voxel size = 0.41 × 0.41 × 4.0 mm³). The color scale limits were identical for all images. The segmentation denotes the voxels used in calculating the signal intensity histograms for the prostate and the liquid marker. As described inSection 2.C.3, only the 25% most centrally located voxels of the 300 μL liquid marker were selected. The prostatic specimen was delineated manually on all slices. The histograms show good contrast between the prostatic tissue and the liquid markers for the T1-weighted image (c)–(d) and the ρ_H-weighted image (e)–(f). The histograms overlap for the T2-weighted image (a)–(b) indicating a lack of image contrast between the liquid markers and the prostate. [Color figure can be viewed at wileyonlinelibrary.com]

the proximity of the marker on CT and CBCT imaging and will augment treatment accuracy.

The characterization of the T2 and T1 relaxation time and the relative proton density ρ_H gives additional insights into the mechanisms behind the appearance of the liquid markers in the *ex vivo* multiparametric MRI images (Fig. 4). Note that these parameters are dependent on the voxel selection criterion and can be influenced by partial volume effects due to the applied slice thickness (4 mm) and the low-relative proton density of the liquid markers. For this reason only, the 25% most centrally located voxels of the largest liquid marker (300 μL, Ø ≈ 8.3 mm) were considered in the quantification of the MRI parameters. The signal intensity of these voxels should correspond to a signal that will be solely determined by the MRI parameters of the liquid marker and should be independent from the gelatin background signal. Note also that the gelatin phantom was designed to be water-equivalent to mimic soft tissue in the kV CT/CBCT and kV x-ray imaging and was not designed to mimic the relaxation times of prostatic tissue in MRI imaging.

A recent study by Schneider et al.[35] quantified the relative proton density ρ_H and the influence of the liquid markers on the magnetic field inhomogeneity ΔB_0. The proton density ρ_H (37 ± 3% with respect to water) determined in our study was larger compared to the value observed by Schneider et al.[35] In addition, in our study, liquid markers showed a larger signal intensity in both T1- and T2-weighted images even though the image sequences were similar to those used by Schneider et al.[35] This is consistent with the larger proton density observed in our study. Liquid marker appearance in T1- and T2-weighted images may be influenced by the difference in magnetic field strength between our study (1.5 T) and Schneider et al.[35] (3.0 T). However, the differences in proton density could also implicate a different liquid marker composition being characterized in our study than the study by Schneider et al.[35]

A chemical shift artifact was observed in the phase-encoding direction of the ADC-map [Fig. 3(d)]. This artifact was caused by a chemical shift of the hydrogen atoms in the liquid marker of 1.02 ppm (31.5 Hz at 1.5 T) with respect to the main resonance frequency. This marker induced artifact will be more pronounced in images with a low BW/pixel value, such as the DWI-SE sequence used in this study (BW/pixel = 20.6 Hz/pixel), and could reduce the visibility of the liquid markers in DWI imaging of the prostate. Note that the large voxel size of the ADC-map (1.3 × 1.3 × 4.0 mm³) and the aforementioned chemical shift artifact limited the amount

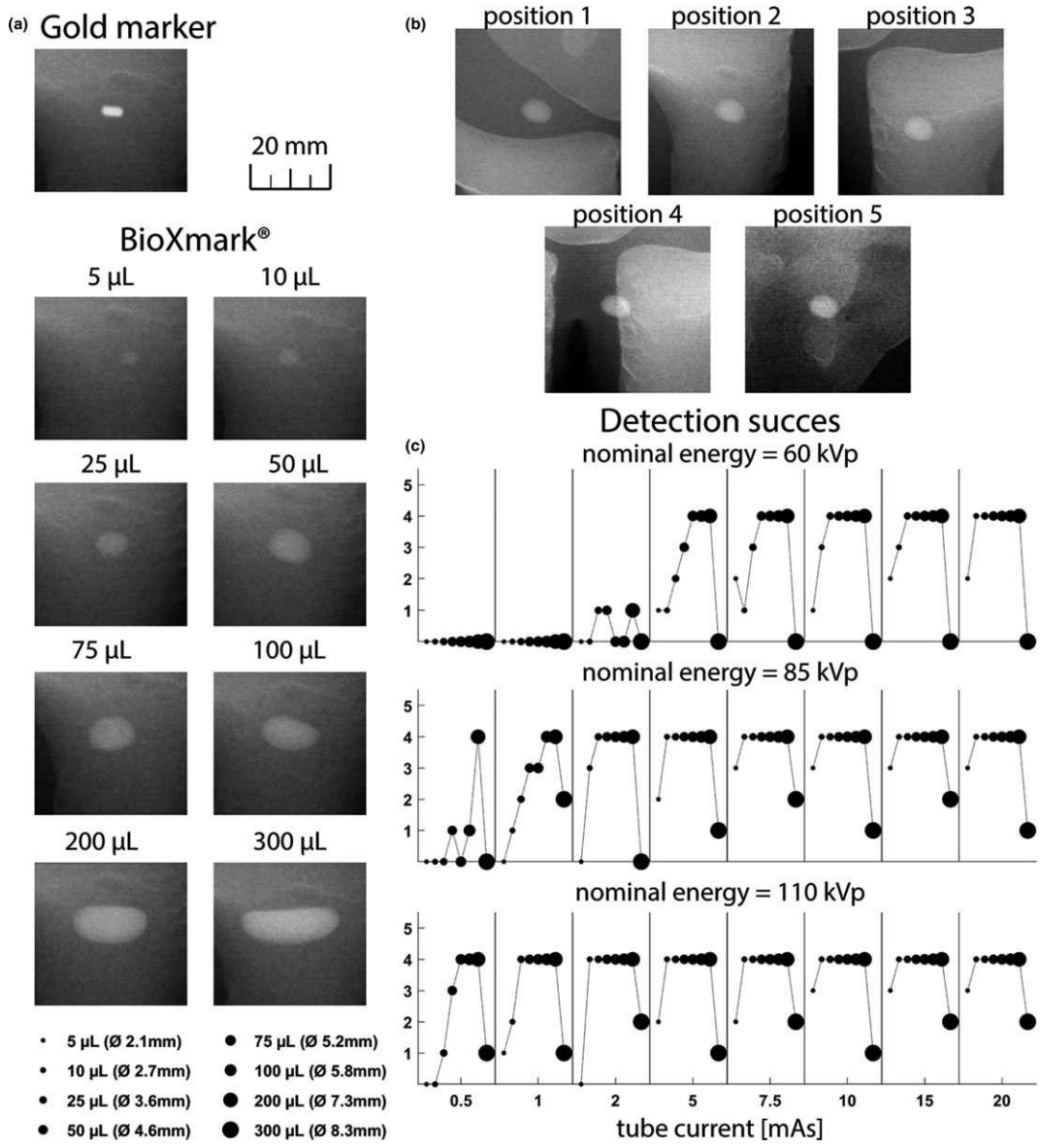

FIG. 5. (a) Visualizes the visibility of the different volumes (5–300 µL) of the liquid marker and the gold fiducial marker in x-ray imaging (nominal energy = 110 kVp, tube current = 15 mAs) with identical window settings and at the same position relative to the pelvic bony anatomy (position 2). (b) Indicates the five different positions relative to the pelvic bony anatomy of the anthropomorphic phantom that was used in this study for the 50 µL marker (nominal energy = 110 kVp, tube current = 15 mAs, different scaling than (a)). (c) Gives the automated detection success of the liquid markers for the different positions and x-ray exposure settings. The smallest marker volumes (5–10 µL) were almost not visible in the x-ray images (a) whereas larger markers (>25 µL) were very noticeable in (a). Automated detection was feasible for liquid marker volumes ranging from 25 to 200 µL (four of five positions). None of the liquid markers was detected successfully for position 4, which lies on a bony structure edge. For reference, the gold markers was detected successfully for all five positions.

of voxels available to determine the mean ADC value of the liquid marker.

When evaluating the *ex vivo* multiparametric MRI sequences, we found that the liquid marker displayed high contrast with respect to the prostatic tissue in the T1-weighted and the ρ_H-weighted images [Figs. 4(c)–4(f)]. However, the liquid markers were not visible in the T2-weighted image as their signal intensities coincided with those of the prostatic tissue [Figs. 4(a)–4(b)]. These results complement the findings by Schneider et al.,[35] which stated that the liquid markers caused signal voids due to their lack of water protons and should equally affect all MRI sequences. However, the lack of contrast in the T2-weighted image indicates that liquid marker visibility in MRI imaging does not solely depend on the low ρ_H value but will also be influenced by the T2 and T1 relaxation times. These will have a non-negligible sequence-dependent influence on the contrast in certain MRI images, such as the T2-weighted image for which the liquid markers were not distinguishable from prostatic tissue.

With exception of the chemical shift artifact in the ADC-map, none of the mp-MRI images displayed imaging artifacts near the liquid markers. This is in line with the small

influence of the liquid markers on the magnetic field inhomogeneity ΔB_0 found by Schneider et al.[35]

One should note that the visibility of the liquid marker in prostatic tissue will depend on the interplay between the marker volume and the voxel size of the MRI image due to the partial volume effect. Hence, it is advisable to use liquid markers that are at least twice the size of the largest voxel size used in the mp-MRI examination.

It should be noted that the obtained signal intensities observed in our *ex vivo* MRI can differ from *in vivo* prostate MRI images due to the influence of temperature[41] and formalin fixation[42] on the T2 and T1 relaxation times of the prostatic specimen. Formalin fixation generally causes a decrease in the T2 and T1 relaxation times. This reduction is most predominant for the T2 relaxation time causing a reduced signal intensity in T2-weighted images. To investigate the influence of the formalin fixation on the acquired *ex vivo* MRI images, we repeated the 2D multiecho SE sequence with identical imaging parameters as in Section 2.C.2 for our prostatic specimen and determined its T2 relaxation time. The obtained T2 relaxation time of 112 ± 40 ms (averaged over the whole prostate gland) is consistent with *in vivo* T2 values described in literature.[43] This indicates that the short exposure (less than 24 h) of the prostatic specimen to formalin will have a minimal impact on the obtained *ex vivo* T2-weighted image.

Liquid markers with a volume of 25–200 μL had successful automated detection (four of five positions) on kV x-ray images, demonstrating their potential usage as a fiducial marker for automated motion monitoring [Fig. 5(c)]. Unfortunately, none of the liquid markers were detected successfully when coinciding with a bony structure edge. This is caused by the low signal intensity of the liquid markers relative to the change in intensity across the bony edge such that the edge has a large impact on the appearance of the liquid marker in the kV x-ray image. In contrast, solid gold markers have a much higher signal intensity such that the impact of the edge is negligible. The normalized cross-correlation–based detection algorithm used in this study has proven to be a reliable detection algorithm for solid fiducial markers[44] but is not adjusted to cope with the influence of the bony structure edge on the signal intensity of the liquid marker. Better adapted marker detection algorithms should be considered for detecting the liquid markers in the presence of bony edges.

In contrast to solid markers, the shape of a liquid marker is not known prior to injection and will highly depend on the actual structure of the surrounding tissue.[33,45] Moreover, the potentially irregular shape of the liquid markers require an angle-specific generation of the template. Consequently, marker templates are ideally patient-specific and generated from a CT or CBCT image with the liquid marker already injected into the prostate.

Patient-specific marker templates must be generated only once as it was previously found that the volumetric shape and structural integrity of the liquid marker remain stable up to 14 weeks,[45] which is ample time when considering prostate SBRT in a 5-week or 2-week period.

Our study showed the wide-ranging applicability of the liquid marker in both multimodal volumetric imaging and kV x-ray–based motion monitoring techniques. Patient-specific marker templates should be generated automatically[46] to optimize the clinical workflow. Moreover, marker localization in the presence of bony edges should be performed with better adapted marker detection algorithms.

Additionally, the liquid marker can also be employed for image guidance in proton therapy as dose perturbations are much smaller compared to solid gold markers.[25]

Furthermore, injection of the liquid markers can be performed using very thin needles (typically 25G) compared to most solid gold markers (typically 18G to 22G). The injected volume can be varied independently from the needle size, leading to the selection of the optimal marker volumes for each patient, disease site, and treatment.

Liquid marker volumes as small as 25 μL were shown to be reliable fiducials in x-ray–based automated marker detection. Moreover, small marker volumes are preferable for CT and CBCT imaging as our study showed that artifact size increased for larger sized markers. However, one should check whether the voxel sizes used in mp-MRI imaging are small enough such that the signal of the liquid markers will not be degraded by the partial volume effect. If this would be the case, one should consider increasing the marker size. For the voxel sizes used in our study, this would correspond to an optimal liquid marker volume of 50 μL. Naturally, each institution should make their own consideration for deducing their optimal liquid marker volume.

5. CONCLUSIONS

This study is the first to show the compatibility of BioXmark® liquid markers with multimodal image-guided radiotherapy for PCa. They displayed favorable results in both visibility and induced imaging artifacts compared to solid gold markers. Liquid marker visibility in MRI imaging of the prostate does not solely depend on the low ρ_H value (not visible on T2-weighted image) but is also influenced by its relaxation times. It was found that automated marker detection in kV x-ray imaging was feasible but better adapted marker detection algorithms are necessary for marker localization in the presence of bony edges. Marker visibility and automated marker detection can be optimized by a patient-specific selection of the optimal liquid marker size by varying the injected volume, always using fine 25G needle size. Hence, the liquid marker provides a minimally invasive and highly applicable alternative to solid gold markers for usage in state-of-the-art multimodal image-guided PCa radiotherapy.

ACKNOWLEDGMENTS

The authors thank Nanovi Radiotherapy A/S for their careful preparation of the gelatin phantom insert containing the different volumes of the BioXmark® liquid marker. The authors also show their gratitude to PEO (PEO Radiation

Technology bvba, Hoogstraten, Belgium) for providing the CIRS Gel Dosimetry Cassette. The authors thank two anonymous referees for their helpful comments. This work was supported by a research grant from Kom op tegen Kanker (Stand up to Cancer), the Flemish Cancer Society.

CONFLICT OF INTEREST

The authors have no conflicts to disclose.

[a)]Authors to whom correspondence should be addressed. Electronic mail: robin.deroover@kuleuven.be; tom.depuydt@kuleuven.be

REFERENCES

1. Arcangeli S, Greco C. Hypofractionated radiotherapy for organ-confined prostate cancer: is less more? *Nat Rev Urol*. 2016;13:400–408.
2. Kishan AU, King CR. Stereotactic body radiotherapy for low- and intermediate-risk prostate cancer. *Semin Radiat Oncol*. 2017;27:268–278.
3. Schild MH, Schild SE, Wong WW, et al. Early outcome of prostate intensity modulated radiation therapy (IMRT) incorporating a simultaneous intra-prostatic MRI directed boost. *Omi J Radiol*. 2014;3:170.
4. Schild MH, Schild SE, Wong WW, et al. A prospective trial of intensity modulated radiation therapy (IMRT) incorporating a simultaneous integrated boost for prostate cancer: long-term outcomes compared with standard image guided IMRT. *Int J Radiat Oncol*. 2017;97:1021–1025.
5. Wortel RC, Incrocci L, Pos FJ, et al. Acute toxicity after image-guided intensity modulated radiation therapy compared to 3D conformal radiation therapy in prostate cancer patients. *Int J Radiat Oncol Biol Phys*. 2015;91:737–744.
6. Murray LJ, Lilley J, Thompson CM, et al. Prostate stereotactic ablative radiation therapy using volumetric modulated arc therapy to dominant intraprostatic lesions. *Int J Radiat Oncol Biol Phys*. 2014;89:406–415.
7. Llis ROJE, Im EDYK, Onant RIC, et al. Radioimmunoguided imaging of prostate cancer foci with histopathological correlation. *Int J Radiat Oncol Biol Phys*. 2001;49:1281–1286.
8. Steenbergen P, Haustermans K, Lerut E, et al. Prostate tumor delineation using multiparametric magnetic resonance imaging: inter-observer variability and pathology validation. *Radiother Oncol*. 2015;115:186–190.
9. Dinh CV, Steenbergen P, Ghobadi G, et al. Multi-center validation of prostate tumor localization using multi-parametric MRI and prior knowledge. *Med Phys*. 2016;44:946–961.
10. Benedict SH, Followill D, Galvin JM, et al. Stereotactic body radiation therapy : The report of AAPM Task Group 101. 2010;(August):4078-4101.
11. Langen KM, Willoughby TR, Meeks SL, et al. Observations on real-time prostate gland motion using electromagnetic tracking. *Int J Radiat Oncol Biol Phys*. 2008;71:1084–1090.
12. Huang CY, Tehrani JN, Ng JA, Booth J, Keall P. Six degrees-of-freedom prostate and lung tumor motion measurements using kilovoltage intrafraction monitoring. *Int J Radiat Oncol Biol Phys*. 2015;91:368–375.
13. Carrara M, Giandini T, Bonfantini F, et al. Analysis of electromagnetic transponders tracking data to quantify intrafraction prostate motion during radiotherapy treatments. *J Phys Conf Ser*. 2017;777:12036.
14. Azcona JD, Xing L, Chen X, Bush K, Li R. Assessing the dosimetric impact of real-time prostate motion during volumetric modulated arc therapy. *Int J Radiat Oncol Biol Phys*. 2014;88:1167–1174.
15. Colvill E, Poulsen PR, Booth JT, O'Brien RT, Ng JA, Keall PJ. DMLC tracking and gating can improve dose coverage for prostate VMAT. *Med Phys*. 2014;41:91705.
16. Colvill E, Booth J, Nill S, et al. A dosimetric comparison of real-time adaptive and non-adaptive radiotherapy: a multi-institutional study encompassing robotic, gimbaled, multileaf collimator and couch tracking. *Radiother Oncol*. 2016;119:159–165.
17. van der Weide L, Admiraal MA, Rosario TS. PO-0889: intra-fraction re-setup with triggered Imaging allows for margin reduction in prostate treatments. *Radiother Oncol*. 2016;119:S427.
18. Keall PJ, Aun Ng J, O'Brien R, et al. The first clinical treatment with kilovoltage intrafraction monitoring (KIM): A real-time image guidance method. *Med Phys*. 2015;42:354–358.
19. Hansen R, Ravkilde T, Worm ES, et al. Electromagnetic guided couch and multileaf collimator tracking on a TrueBeam accelerator. *Med Phys*. 2016;43:2387–2398.
20. Fast MF, O'Shea TP, Nill S, Oelfke U, Harris EJ. First evaluation of the feasibility of MLC tracking using ultrasound motion estimation. *Med Phys*. 2016;43:4628–4633.
21. Pathmanathan AU, van As NJ, Kerkmeijer LGW, et al. MRI-guided adaptive radiotherapy; a "game changer" for prostate radiotherapy. *Int J Radiat Oncol Biol Phys*. 2017;100:361–373.
22. Ng M, Brown E, Williams A, Chao M, Lawrentschuk N, Chee R. Fiducial markers and spacers in prostate radiotherapy: current applications. *BJU Int*. 2014;113(SUPPL. 2):13–20.
23. Iğdem Ş, Akpinar H, Alço G, Ağaçayak F, Turkan S, Okkan S. Implantation of fiducial markers for image guidance in prostate radiotherapy: patient-reported toxicity. *Br J Radiol*. 2009;82:941–945.
24. Loh J, Baker K, Sridharan S, et al. Infections after fiducial marker implantation for prostate radiotherapy: are we underestimating the risks? *Radiat Oncol*. 2015;10:38.
25. Scherman RJ, Perrin R, Jølck RI, et al. Liquid fiducial marker applicability in proton therapy of locally advanced lung cancer. *Radiother Oncol*. 2017;122:393–399.
26. Cheung J, Kudchadker RJ, Ronald Zhu X, Lee AK, Newhauser WD. Dose perturbations and image artifacts caused by carbon-coated ceramic and stainless steel fiducials used in proton therapy for prostate cancer. *Phys Med Biol*. 2010;55:7135–7147.
27. Hargreaves BA, Worters PW, Pauly KB, Pauly JM, Koch KM, Gold GE. Metal-induced artifacts in MRI. 2011;(September):547–555.
28. Gurney-Champion OJ, Lens E, van der Horst A, et al. Visibility and artifacts of gold fiducial markers used for image guided radiation therapy of pancreatic cancer on MRI. *Med Phys*. 2015;42:2638–2647.
29. Rylander S, Thörnqvist S, Haack S, et al. Intensity profile based measurement of prostate gold markers influence on 1. 5 and 3T diffusion-weighted MR images. 2011;(August 2017).
30. Chai X, van Herk M, van de Kamer JB, et al. Behavior of lipiodol markers during image guided radiotherapy of bladder cancer. *Int J Radiat Oncol Biol Phys*. 2010;77:309–314.
31. Søndergaard J, Olsen KØ, Muren LP, Elstrøm UV, Grau C, Høyer M. A study of image-guided radiotherapy of bladder cancer based on lipiodol injection in the bladder wall. *Acta Oncol (Madr)*. 2010;49:1109–1115.
32. Dudouet P, Portalez D, Lhez JM, et al. Trans-rectal ultrasonography (TRUS) with lipiodol injection for localization of the prostatic apex before radiotherapy planning. *Radiother Oncol*. 2001;61:135–141.
33. Rydhög JS, Mortensen SR, Larsen KR, et al. Liquid fiducial marker performance during radiotherapy of locally advanced non small cell lung cancer. *Radiother Oncol*. 2016;121:64–69.
34. Rydhog JS, Jolck RI, Andresen TL, af Rosenschold PM. Quantification and comparison of visibility and image artifacts of a new liquid fiducial marker in a lung phantom for image-guided radiation therapy. *Med Phys*. 2015;42:2818–2826.
35. Schneider S, Jolck RI, Troost C, Hoffmann AL. Quantification of MRI visibility and artifacts at 3T of liquid fi ducial marker in a pancreas tissue-mimicking phantom. *Med Phys*. 2017;45:37–47.
36. Jølck RI, Binderup T, Hansen AE, et al. Injectable colloidal gold in a sucrose acetate isobutyrate gelating matrix with potential use in radiation therapy. *Adv Healthc Mater* 2014;3:1680–1687.
37. Jølck RI, Rydhög JS, Christensen AN, et al. Injectable colloidal gold for use in intrafractional 2d image-guided radiation therapy. *Adv Healthc Mater*. 2015;4:856–863.
38. Captur G, Gatehouse P, Keenan KE, et al. A medical device-grade T1 and ECV phantom for global T1 mapping quality assurance — the T 1 Mapping and ECV Standardization in cardiovascular magnetic resonance (T1MES) program. *J Cardiovasc Magn Reson*. 2016;18:1–20.
39. Elen A, Isebaert S, De Keyzer F, et al. Validation of an improved patient-specific mold design for registration of in-vivo MRI and

histology of the prostate. In: Shekhar R, Wesarg S, González BM, et al., eds. *Clinical Image-Based Procedures*. Translational Research in Medical Imaging: 5th International Workshop, CLIP 2016, Held in Conjunction with MICCAI 2016, Athens, Greece, October 17, 2016, Proceedings. Cham: Springer International Publishing; 2016:36–43.

40. Barral JK, Gudmundson E, Stikov N, Etezadi-amoli M, Stoica P, Nishimura DG. A robust methodology for in vivo T 1 mapping. *Magn Reson Med*. 2010;64:1057–1067.
41. Thelwall PE, Shepherd TM, Stanisz GJ, Blackband SJ. Effects of temperature and aldehyde fixation on tissue water diffusion properties, studied in an erythrocyte ghost tissue model. *Magn Reson Med*. 2006;56:282–289.
42. McGrath DM, Lee J, Foltz WD, et al. MR elastography to measure the effects of cancer and pathology fixation on prostate biomechanics, and comparison with T1, T2and ADC. *Phys Med Biol*. 2017;62:1126–1148.
43. Roebuck JR, Haker SJ, Mitsouras D, Rybicki FJ, Tempany CM, Mulkern RV. Carr-Purcell-Meiboom-Gill imaging of prostate cancer: quantitative T2 values for cancer discrimination. *Magn Reson Imaging*. 2009;27:497–502.
44. Harris EJ, McNair HA, Evans PM. Feasibility of fully automated detection of fiducial markers implanted into the prostate using electronic portal imaging: a comparison of methods. *Int J Radiat Oncol Biol Phys*. 2006;66:1263–1270.
45. Jølck R, Hansen AE, Andresen TL. PO-0782: BioXmark(TM) ñ a liquid injectable fiducial marker for image guided radiotherapy. *Radiother Oncol*. 2014;111:S52.
46. Bertholet J, Wan H, Toftegaard J, et al. Fully automatic segmentation of arbitrarily shaped fiducial markers in cone-beam CT projections. *Phys Med Biol*. 2017;62:1327–1341.